Epitaxial growth and stoichiometry control of pyrochlore $Nd_2Ru_2O_7$ thin films

K. S. Rabinovich, G. Kim, A. N. Yaresko, G. Christiani, G. Logvenov, B. Keimer, and A. V. Boris*
Max-Planck-Institute for Solid State Research, Heisenbergstrasse 1, 70569 Stuttgart, Germany

(Received 20 December 2023; accepted 15 April 2024; published 1 May 2024)

We report on the epitaxial growth of pyrochlore NRO thin films utilizing a reactive off-axis sputtering technique. The growth process employed Ru and Nd metal targets with a repetitive substrate temperature sequence. X-ray diffraction, magnetic susceptibility, and spectroscopic ellipsometry measurements confirm that the structural, magnetic, and electronic properties of near-stoichiometric NRO films match those of the bulk material. Our spin-polarized density functional calculations based on $Nd_2Ru_2O_7$ structural parameters accurately describe the optical spectra and assign Hubbard bands to the interband transitions observed above the optical band gap of 0.2 eV. By utilizing the technique's capability to adjust the degree of ruthenium deficiency, we investigated $Nd_2Ru_2O_7$ films across a wide range of stoichiometric variations. Decreasing the Ru/Nd ratio results in lattice expansion, an increase in the optical band gap, and the suppression of Ru 4*d* intersite optical transitions. Additionally, this adjustment facilitates the elimination of minor inclusions of a ferromagnetic NdO_x impurity phase, influencing the magnetic properties of stoichiometric films at low temperatures. The successful growth of $Nd_2Ru_2O_7$ films opens up promising opportunities for designing and exploring strain- and light-induced states in pyrochlore ruthenates.

DOI: 10.1103/PhysRevMaterials.8.053801

I. INTRODUCTION

Metal oxides with the pyrochlore structure have played prominent roles in a diverse set of research areas ranging from electrocatalysis [1,2] to geometrically frustrated magnetism [3,4] and topological metallicity [5]. 4*d*- and 5*d*-metal oxides such as ruthenates and iridates with composition $A_2(Ru,Ir)_2O_7$ (*A* is usually a rare earth or alkaline earth metal) are of particular interest because the intraatomic spin-orbit coupling is comparable to the electronic correlation strength, giving rise to multiple nearly degenerate electronic phases with unusual chemical and physical properties. This degeneracy implies that even minor distortions of the crystal lattice or slight external stimuli, such as illumination and electric field, can greatly influence the phase behavior and macroscopic properties. Thin-film structures offer a powerful platform for manipulation and control of the lattice structure and electron system in such compounds, as the crystallographic bond lengths and bond angles can be tuned via epitaxial strain, the electronic dimensionality via the film thickness, and the charge carrier concentration via nonequilibrium drive or interfacial charge transfer in heterostructures. A large-scale effort has therefore been undertaken to synthesize thin films of pyrochlore iridates, which exhibit signatures of quantum spin-liquid and topological semimetallic phases in bulk form [6–10].

Pyrochlore ruthenates are equally interesting in view of their unusual physical [11–13] and chemical [2,14] properties, but their investigation is less advanced, partly reflecting difficulties in synthesizing single crystals and thin films with controlled stoichiometry. The synthesis of high-quality ruthenate films has been challenging, primarily due to the volatility of ruthenium oxides, leading to a ruthenium deficiency and the creation of its vacancies in the film. To tackle this issue, we have developed a modified reactive off-axis sputtering technique illustrated in Fig. 1(a). Our method involves using two sputtering guns of adjustable power with *A* and Ru metal targets in a mixed Ar/O_2 atmosphere to achieve an excess flux of elemental ruthenium during film growth to compensate the high volatility of ruthenium oxides. Ar and O_2 gases are employed as sputter and reactive gas, respectively, where oxygen plasma oxidizes metal particles sputtered by the Ar ions. This method represents a further advancement of our previous approach, which has proven successful in growing films of perovskite ruthenates [15–17]. The substrate is placed off axis from the metal targets to reduce impinging particles' energy [18]. We also control and cycle the substrate temperature within a specific range [Fig. 1(b)] to stabilize the growth of the pyrochlore phase.

In this manuscript, we demonstrate the reliability and advantages of this technique through the growth of epitaxial films of the well-studied $A = Nd$ pyrochlore ruthenate $Nd_2Ru_2O_7$ [19–22]. By systematically varying the deposition conditions, we trace the influence of a ferromagnetic NdO_x impurity phase and the formation of ruthenium vacancies on the films' structural, magnetic, and electronic properties. Our

*A.Boris@fkf.mpg.de

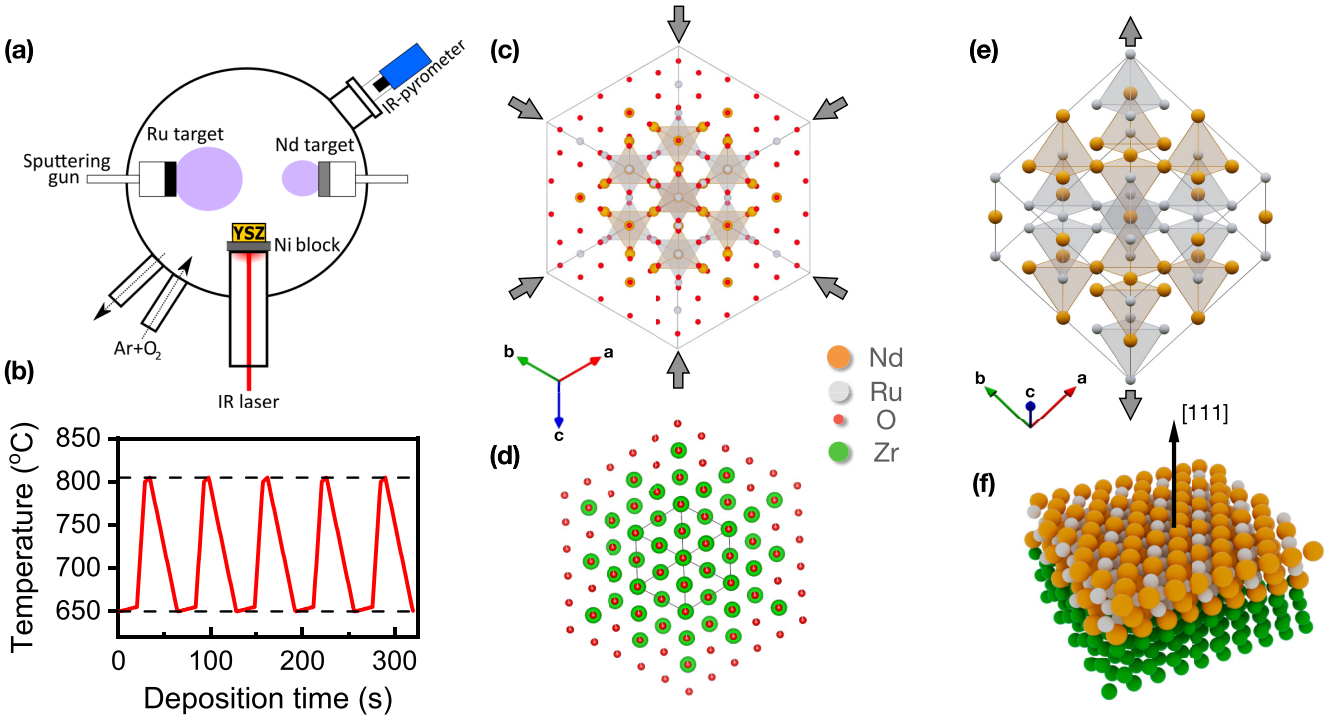

FIG. 1. (a) Schematic of the off-axis reactive sputtering chamber. (b) Substrate temperature profile applied during the thin film growth process. (c), (d) Projection along the [111] direction for $Nd_2Ru_2O_7$ pyrochlore (c) and YSZ fluorite (d) structures, with the unit cell edges depicted by thin solid lines. (e) Corner-sharing Nd (orange balls) and Ru (gray balls) tetrahedra within the pyrochlore lattice. The body diagonal of the cubic unit cell aligns with the film growth [111] direction. (f) Schematic illustration of $Nd_2Ru_2O_7$ deposition on YSZ. Gray arrows in (c) and (e) illustrate the strain-induced distortion of the pyrochlore lattice.

x-ray diffraction, magnetic susceptibility, and spectroscopic ellipsometry measurements validate that the properties of near stoichiometric $Nd_2Ru_2O_7$ films match those of the bulk material.

II. METHODS

Pyrochlore ruthenate $Nd_2Ru_2O_7$ epitaxial films are synthesized on Y_2O_3(9.5 mol %) -stabilized ZrO_2 (YSZ) (111) single-crystal substrates from CrysTec GmbH. YSZ takes a cubic CaF_2-type structure with a lattice constant of 5.13 Å, which is compatible with the $Nd_2Ru_2O_7$ structure, as illustrated in Figs. 1(c) and 1(d). The doubled lattice parameter of YSZ is approximately 1% smaller than the $Nd_2Ru_2O_7$ bulk value of 10.3544(5) Å [21,22], resulting in slight compressive in-plane strain. The use of YSZ as a substrate has recently shown success in growing thin films of pyrochlore iridates [7,10,23–25]. The substrate is mounted to a pure nickel block using platinum paste and subjected to controlled heating using an infrared laser. The substrate temperature is monitored using an infrared (IR) radiation pyrometer. The films are deposited in a mixed Ar/O_2 atmosphere at a total pressure of 100 mTorr, with a partial oxygen pressure of 21 mTorr. Two Nd and Ru metal targets with 33 mm diameter are held in sputtering guns from MeiVac. These targets are symmetrically positioned off axis relative to the substrate, spaced 10 to 20 cm apart. The relative power ratio supplied to the sputtering guns, ranging from 1:1 to 2:1 for the Ru and Nd targets, respectively, controls the relative amount of material sputtered, which enables accurate adjustment of the composition and properties of the deposited thin films. The radio frequency power supplied to the Ru sputtering gun is set at $Ru^W = 45$ W.

To maintain the stability of the pyrochlore phase, the sputtering procedure employs a repetitive temperature sequence ($650\,^\circ\text{C} \xrightarrow{20\text{ sec.}} 655\,^\circ\text{C} \xrightarrow{9\text{ sec.}} 800\,^\circ\text{C} \xrightarrow{5\text{ sec.}} 805\,^\circ\text{C} \xrightarrow{30\text{ sec.}} 650^\circ\text{C}$), as illustrated in Fig. 1(b). During the initial ~20 second phase of film growth at a substrate temperature of 650 °C, ruthenium exhibits minimal volatility, yet significant structural disorder exists. Conversely, ruthenium becomes notably volatile in the form of RuO_x when maintaining the substrate temperature close to 800 °C for the subsequent ~10 seconds. However, thermodynamics' control of film stoichiometry at high temperatures effectively reduces disorder and enhances film crystallinity. Employing an empirically chosen sequence enables us to grow high-quality $Nd_2Ru_2O_7$ films.

The structure of the films was analyzed by high-resolution x-ray diffraction (XRD) using a CuK-α source ($\lambda = 1.5406$ Å). To assess the relative content of Ru and Nd cations, we recorded energy-dispersive x-ray (EDX) spectra with a NORAN System 7 (NSS212E) detector in a Tescan Vega (TS-5130MM) scanning electron microscope (SEM). Magnetic properties were measured using a SQUID-based magnetometer (Quantum Desing Co. MPMS3) in the 10 K–300 K temperature range. Spectroscopic ellipsometry measurements were made at room temperature in the photon energy range of 0.5 eV–6.5 eV with a rotating analyzer type variable-angle spectroscopic ellipsometer (VASE) from Woollam Co. Inc. Both the real and imaginary parts of the complex dielectric function, $\tilde{\varepsilon}(\omega) = \varepsilon_1(\omega) + i\varepsilon_2(\omega) = 1 + 4\pi i[\sigma_1(\omega)$

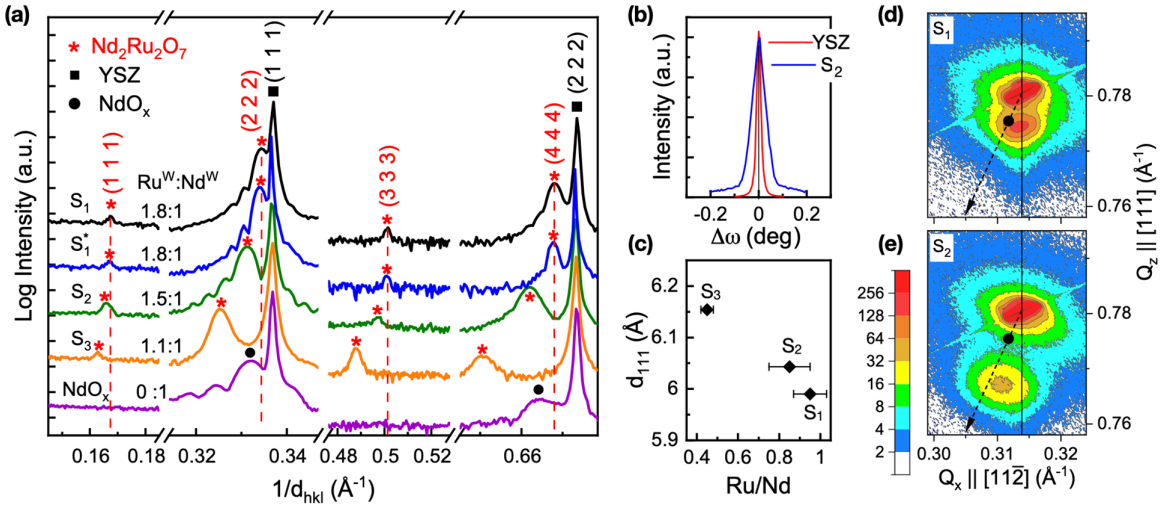

FIG. 2. (a) X-ray diffraction patterns of $Nd_2Ru_2O_7$ films deposited on a YSZ (111) substrate using different power ratios for the Ru and Nd sputtering guns ($Ru^W : Nd^W$). The lattice spacing $d_{hkl} = \lambda/2\sin\theta$, where $\lambda = 1.5406$ Å, and θ represents the Bragg angle. The vertical dashed lines indicate the positions of (111), (222), (333), and (444) reflections in the S_1 film, serving as a reference. (b) Rocking curves of the $Nd_2Ru_2O_7$ (222) and YSZ (111) peaks. (c) Out-of-plane lattice spacing, determined from the peak positions in (a), as a function of the Ru/Nd ratio determined by EDX. (d), (e) Reciprocal space maps around the $Nd_2Ru_2O_7$ (662) and YSZ (331) peaks of the S_1 (d) and S_2 (e) films. The black vertical lines indicate the in-plane (Q_x) position of the YSZ (331) reflection. The reciprocal spacing of strain-free cubic $Nd_2Ru_2O_7$ is indicated by the black circles. The dashed-line arrows point toward the origin.

$+ i\sigma_2(\omega)]/\omega$, were directly obtained by numerically inverting the ellipsometric angles Ψ and Δ measured at different angles of incidence ranging from 60° to 75°. The inversion was performed using a best-match single-film model calculation procedure implemented in the Woollam WVASE software [26]. Infrared absorption spectra were recorded in transmission mode using Bruker's VERTEX 80v Fourier transform IR spectrometer, down to a photon energy of 0.15 eV. The optical spectra were described using first-principles band structure calculations performed for the experimental structural parameters of bulk $Nd_2Ru_2O_7$ [22]. The Coulomb interaction of Ru $4d$ electrons in the presence of spin-orbit coupling (SOC) was accounted for using the rotationally invariant DFT+U method [27], as implemented in the PY LMTO computer code [28]. Nd^{3+} $4f^3$ states were treated as semicore states and their spin polarization was neglected. The interband contribution to the imaginary part of the dielectric tensor was calculated using the dipole approximation for the momentum operator matrix elements [28].

III. RESULTS AND DISCUSSIONS

We successfully fabricated a series of films with distinct characteristics by adjusting the relative proportions of sputtered Ru and Nd metals. Based on their properties, these films can be categorized into three groups, represented by films S_1 (S_1^*), S_2, and S_3. Films S_1 and S_1^* were grown under the same conditions. The $Ru^W : Nd^W$ power ratio of 1.8:1, 1.5:1, and 1.1:1 was applied for films S_1 (S_1^*), S_2, and S_3, respectively. Thin films S_1, S_1^* (36.5 nm), and S_2 (28.8 nm) were deposited at a rate of 1 Å/s. The distance between the Ru and Nd targets during deposition was set to 20 cm. The thicker S_3 (140.7 nm) film was deposited at a faster rate of 4.8 Å/s with the metal targets spaced closer together at a distance of 10 cm.

Figure 2(a) presents the XRD patterns obtained from the out-of-plane reflections of the $Nd_2Ru_2O_7$ films. The lattice parameters were determined by refining the XRD data using (111), (222), (333), and (444) Bragg reflections within the face-centered cubic pyrochlore structure with the space group $Fd\bar{3}m$ [20–22]. The absence of additional reflections indicative of extrinsic phases confirms the phase-pure growth of the films within the accuracy of the XRD measurements. The finite size fringes clearly defined around the (222) reflection indicate uniform film quality with a sharp interface between the film and substrate and a smooth film surface. The high film quality is further confirmed by the observation of a typical rocking curve around the (222) peak [Fig. 2(b)] with a full width at half maximum (FWHM) of approximately 0.07°. Figure 2(c) shows that the out-of-plane lattice spacing in the films increases as the atomic ratio between Ru and Nd decreases. The Ru/Nd ratio was determined by averaging the ratio of element-specific peak intensities in the EDX spectra over tens of measured spots across the entire film surface. The overlap of the Ru peak with the Zr peak of the YSZ substrate results in larger standard deviations, depicted as error bars in Fig. 2(c), particularly noticeable for thinner films. The comparative analysis of reciprocal space mapping (RSM) around the $Nd_2Ru_2O_7$ (662) and YSZ (331) peaks from the film and the substrate, respectively, as shown in Figs. 2(d) and 2(e), provides insight into the strain state of the films. In Fig. 2(d), both peaks align along the same Q_x, indicating that film S_1, grown coherently on the substrate, remains strained. The smaller Q_x vector of the $Nd_2Ru_2O_7$ (662) reflection from film S_2 suggests strain relaxation, attributed to lattice expansion resulting from Ru deficiency in the film. Despite the increase in lattice parameters, the relative position of the $Nd_2Ru_2O_7$ (662) peak with respect to the undistorted cubic lattice line [indicated by dotted-line arrows in Figs. 2(d) and 2(e)] remains nearly the same. This similarity suggests that

the strain-induced distortions illustrated in Figs. 1(c) and 1(e) persist similarly for both films S_1 and S_2.

In films S_1 and S_1^* grown under conditions of the highest excess flux of elemental ruthenium, possible deviation from stoichiometry does not exceed the estimated error bar of the EDX analysis. The lattice structure of these films is close to a pyrochlore cubic lattice, with a lattice parameter of $a = 10.36$ Å. However, it exhibits a slight elongation of 0.1% along the [111] out-of-plane direction and a compression of 0.5% along the [11$\bar{2}$] in-plane direction. The obtained lattice parameter value closely aligns with the bulk value of 10.3544(5) Å [21,22], further indicating the high stoichiometry of films S_1 and S_1^*. Reducing the Ru^W:Nd^W ablation ratio to 1.5:1 results in a 10–15% decrease in the Ru/Nd ratio. Consequently, the lattice parameter of film S_2 increases to 10.45 Å. The out-of-plane and in-plane structural distortions remain nearly unchanged at +0.18% and −0.55%, respectively. To demonstrate the high Ru deficiency in the film grown under parity ablation conditions for Ru and Nd ions, we further reduced the ablation ratio to 1.1:1. Even with the estimated Ru/Nd ratio in S_3 films reaching values as low as 0.5, the film retains a pyrochlore structure with a lattice constant as large as 10.65 Å. Recent theoretical and experimental evidence supports the pyrochlore structure's capacity to effectively accommodate a high density of defects, adapting to A-site excess through the formation of antisite defects, with their charge compensated by oxygen vacancies [29,30]. The increase in the density of these defects accounts for the shift toward lower angles in the XRD pattern [30,31]. The observed lattice expansion at lower ruthenium content is also consistent with findings in perovskite ruthenates, where a reduction in charge screening due to Ru vacancies contributes to an increase in the volume of the unit cell [32].

The magnetic properties of polycrystalline $Nd_2Ru_2O_7$ are governed by the antiferromagnetic ordering of Ru^{4+} 4*d* spins at $T_N = 146$ K. This ordering leads to a distinct splitting between the zero-field-cooled (ZFC) and field-cooled (FC) magnetic susceptibility curves, resulting from a minor cusplike feature observed in the ZFC curve [19–22]. This characteristic feature has been detected in films S_1, S_1^*, and S_2, albeit at slightly lower temperatures compared to previous reports. The inset in Fig. 3(c) illustrates a weak but consistently reproducible feature characteristic of $Nd_2Ru_2O_7$ polycrystals at T_N. Although observed in S_2, it could not be detected unambiguously in film S_3. The magnetic susceptibility measurements of thin films do not provide sufficient information to determine the specific ordering of Ru 4*d* spins in $Nd_2Ru_2O_7$. Further investigations on pyrochlore ruthenate thin films would be particularly valuable in exploring the influence of strain and nonstoichiometry on magnetic order, especially considering the accompanying geometric frustration. Advanced local magnetic probes would be necessary to address this issue.

Figure 3 illustrates that the most noticeable difference in the magnetic properties of films S_1 and S_1^* from S_2 and S_3 lies in the low-temperature behavior. Films S_1 and S_1^* exhibit a particularly prominent divergence between the ZFC and FC curves, primarily attributed to a broad feature at 45 K in the ZFC curve. Sample S_1^* shows a more pronounced effect even though it was grown under the same conditions as sample S_1.

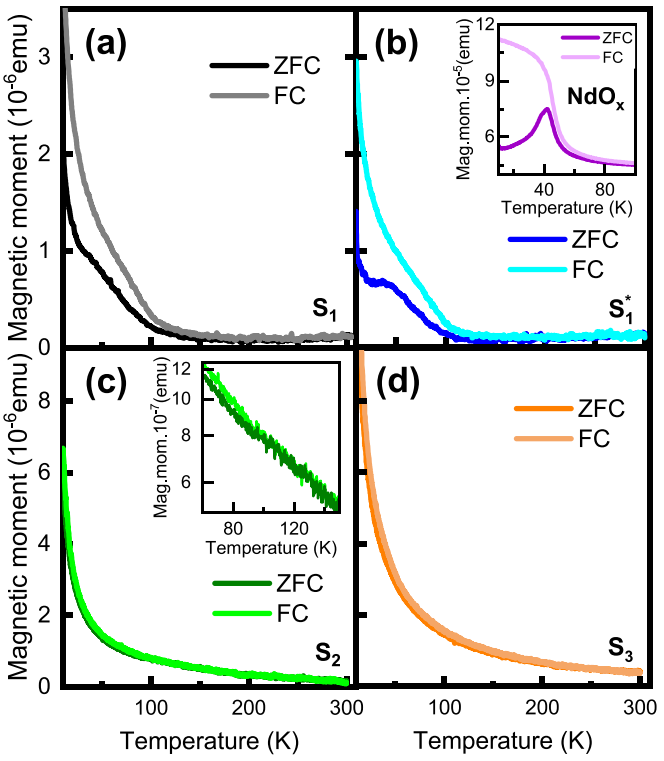

FIG. 3. Zero-field-cooled (ZFC) and field-cooled (FC) temperature dependence of magnetic moment M for $Nd_2Ru_2O_7$ films (a) S_1, (b) S_1^*, (c) S_2, (d) S_3. A magnetic field of 1000 Oe was applied in the film plane ($H_\parallel$). Color coding of the ZFC curves corresponds to the XRD patterns in Fig. 2(a). Insets: (b) M of the reference NdO_x film, (c) enlargement near the magnetic transition.

In contrast, films grown with a lower Ru^W : Nd^W ablation ratio do not display this low-temperature anomaly. The behavior and manifestation of this anomaly resemble the characteristics of a similar low-temperature anomaly observed at 21 K in the dc magnetic susceptibility of certain polycrystalline $Nd_2Ru_2O_7$ samples [21,22]. However, the precise causes underlying this anomaly remain uncertain. According to Ku *et al.*, the observed effect may suggest the potential emergence of a weak ferromagnetic component resulting from the canting of the ordered Ru moments [22]. This canting is attributed to the weak exchange coupling with the Nd moments, which become polarized at low temperatures. However, the nonreproducibility of the low-temperature feature in the magnetic susceptibility curves among different polycrystalline samples [20] and films S_1 and S_1^*, as well as the absence of any notable accompanying features near this temperature in the heat capacity and neutron diffraction data [22], suggest that it is attributed to minute ferromagnetic impurities, which do not manifest in the XRD patterns in Fig. 2(a).

To address this issue, we grew NdO_x films under the same conditions but with the complete blocking of the ruthenium flow. The XRD pattern obtained from the out-of-plane reflections of the NdO_x film is consistent with the cubic rock salt crystal structure (space group $Fm\bar{3}m$). The determined lattice constant of 5.22 Å closely matches the values reported for ferromagnetic epitaxial NdO films, ranging from 5.05 Å to 5.16 Å [33]. Recent reports have demonstrated intrinsic

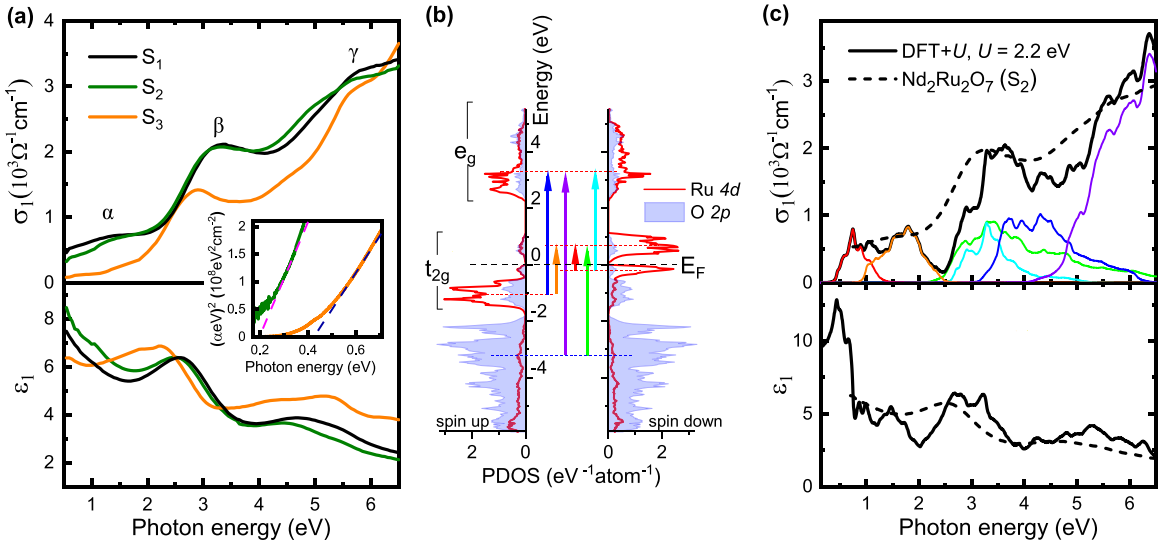

FIG. 4. (a) Real part of the optical conductivity $\sigma_1(\omega)$ (upper panel) and dielectric permittivity $\varepsilon_1(\omega)$ (bottom panel) of $Nd_2Ru_2O_7$ measured on films S_1, S_2, and S_3 at room temperature ($T = 293$ K). Color coding of the $\sigma_1(\omega)$ and $\varepsilon_1(\omega)$ curves corresponds to the XRD patterns in Fig. 2(a). The inset shows the Tauc plot obtained from the infrared absorption spectra. The linear fit (dashed lines) yields direct band gaps of 0.2 eV and 0.45 eV for samples S_2 and S_3, respectively. (b) Partial densities of the majority spin (spin up, left panel) and minority spin (spin down, right panel) Ru $4d$ states (red lines) and oxygen O $2p$ states (blue shaded areas) calculated by DFT+U assuming antiferromagnetic order [37]. The calculations utilize the crystal structure of bulk $Nd_2Ru_2O_7$ [22]. The colors of the vertical arrows indicate the orbital character of the corresponding optical bands. (c) Real part of the optical conductivity $\sigma_1(\omega)$ (upper panel) and dielectric permittivity $\varepsilon_1(\omega)$ (bottom panel) calculated by DFT+U (thick black lines) with a breakdown into separate orbital contributions (thin colored lines). The colors of the separate bands correspond to the electronic transitions depicted by the arrows in (b). The dashed lines correspond to the experimental S_2 spectra in (a).

ferromagnetism in strained epitaxial NdO and NdN thin films, where the ferromagnetic ordering of the Nd moments occurs at T_C of approximately 19 K and 43 K, respectively [33,34]. In Fig. 3(b), the inset depicts the temperature dependence of magnetic moment for the reference NdO_x film. The behavior of the FC and ZFC curves closely resembles that reported for ferromagnetic NdO and NdN thin films: The FC curve exhibits an upturn and subsequent saturation below 50 K, while the ZFC curve diverges significantly from the FC curve, sharply dropping below 40 K. The observed drop indicates that the applied field of 1000 Oe falls below the coercive field at temperatures below the critical temperature. Based on this supplementary finding, we confidently assert that the low-temperature magnetic properties of films S_1 and S_1^* are indeed significantly influenced by the presence of a ferromagnetic NdO_x impurity phase. Conversely, films S_2 and S_3 do not exhibit any indications of a low-temperature ferromagnetic response. It may seem inconsistent that a relative increase in Nd flux suppresses the secondary NdO_x phase. However, it is essential to emphasize that the lattice mismatch for $Nd_2Ru_2O_7$ films S_1 and S_1^* relative to twice the bulk NdO lattice constant [35] is 3.6%, whereas for films S_2 and S_3 it exceeds 4.5% and 6.5%, respectively, falling outside the typical range of strain that oxides can tolerate [36]. This observation suggests that the elastic strain energy caused by the misfit between the $Nd_2Ru_2O_7$ and NdO crystal lattices impedes the growth of the NdO_x phase in the matrix of ruthenium-deficient $Nd_2Ru_2O_7$ films S_2 and S_3. Consequently, this provides an effective means to control the ferromagnetic impurity.

We measured the dielectric response of the fabricated films to investigate the influence of Ru vacancies and the resulting lattice expansion on the electrodynamics and electronic structure of $Nd_2Ru_2O_7$. Figure 4(a) presents the optical conductivity and dielectric permittivity spectra for films S_1, S_2, and S_3, determined through spectroscopic ellipsometry measurements from infrared to ultraviolet at room temperature. The observed optical bands can be categorized into three distinct groups labeled as α, β, and γ. These optical bands remain largely unchanged from sample S_1 to sample S_2. However, the spectra of sample S_3 show very significant suppression of the α and β bands, accompanied by a red shift in the β bands. Additionally, the direct band gap increases from 0.2 eV to 0.45 eV, as depicted in the inset of Fig. 4(a) for films S_2 and S_3. In film S_1, the absorption edge falls within the YSZ absorption bands between 0.14 eV and 0.2 eV [38].

To assign the observed optical bands, we compared the experimental spectra with relativistic DFT+U calculations. Figures 4(b) and 4(c) present the calculated partial densities of states (PDOS) for Ru $4d$ and oxygen $2p$ states, along with the corresponding optical spectra. The calculations were performed using the experimental structural data for bulk $Nd_2Ru_2O_7$ [22], assuming a noncollinear AF ordering of the Ru^{4+} $4d$ spins perpendicular to $\langle 111 \rangle$ directions consistent with neutron diffraction data [37]. The total energy calculated for the magnetic structure is lower than the energy of all-in-all-out magnetic order with Ru spins parallel to $\langle 111 \rangle$ local trigonal axes. With the Hund's coupling fixed to $J_H = 0.8$ eV, we found that $U = 2.2$ eV gives the best match of the calculated absorption peaks with the experimental spectra. The calculations revealed a Mott gap that separates two unoccupied Ru $t_{2g\downarrow}$ states from the occupied minority spin $t_{2g\downarrow}$ state with the orbital momentum $l_z = -1$. The computed band gap of 0.2 eV agrees fairly well with the experimentally detected one in films S_1 and S_2, which is also consistent with the

TABLE I. Comparison of $Nd_2Ru_2O_7$ films grown with different $Ru^W : Nd^W$ power ratios.

S no.	$Ru^W : Nd^W$	Ru/Nd	d_{111} (Å)	T_N[a] (K)	FM imp.	$t_{2g} \rightarrow t_{2g}$
S_1, S_1^*	1.8:1	0.95 ± 0.08	5.99	130 ± 15	√	√
S_2	1.5:1	0.85 ± 0.10	6.04	95 ± 10	×	√
S_3	1.1:1	0.45 ± 0.04	6.15	N/A	×	×

[a]T_N is estimated based on the point of divergence of the ZFC and FC curves in Fig. 3.

activation energy obtained from the temperature-dependent dc conductivity measurements on polycrystalline $Nd_2Ru_2O_7$ [39].

We assign the α absorption band to weakly allowed Ru $4d$ transitions between neighboring sites i and j, given by $t_{2g}^4(i)\ t_{2g}^4(j) \rightarrow t_{2g}^3(i)\ t_{2g}^5(j)$. In the final low-spin $S = 1/2$ local excited state, an electron is transferred to one of the unoccupied $t_{2g\downarrow}$ states. The β absorption band is near equally contributed by both Ru $4d$ $t_{2g} \rightarrow e_g$ and charge transfer O $2p \rightarrow$ Ru t_{2g} transitions. The γ band arises from charge transfer O $2p \rightarrow$ Ru e_g transitions at higher energy. Significantly, the spectra of film S_3 reveal a remarkable suppression of the weakly allowed Ru $4d$ transitions, indicating a high degree of Ru deficiency that profoundly impacts the electronic structure of $Nd_2Ru_2O_7$. The severely reduced Ru site occupancy leads to an over-proportional decrease in the probability of $t_{2g} \rightarrow t_{2g}$ transitions between neighboring sites due to significant changes in the initial and final PDOS and corresponding matrix elements. In film S_3, this transition probability becomes negligible in the absence of Ru at a neighboring site.

Table I summarizes the structural, magnetic, and electronic properties of the films grown at different power ratios supplied to the Ru and Nd sputtering guns. The selected films most effectively demonstrate how the properties change with adjustments in the Ru^W:Nd^W ablation ratio. In the growth of films S_1 and S_1^*, we successfully fabricated nearly stoichiometric $Nd_2Ru_2O_7$ films with a lattice structure that closely aligns with a pyrochlore cubic lattice of polycrystalline $Nd_2Ru_2O_7$. However, the magnetic properties of these films are noticeably affected by the presence of ferromagnetic NdO_x impurities in minute quantities, which do not manifest in the XRD and optical data. Films S_2 and S_3 lack these impurities. Growing film S_3 demonstrates that a pyrochlore structure can be retained even under parity ablation conditions for Ru and Nd ions, accommodating a high density of defects such as Nd-Ru antisite defects and oxygen vacancies. Unlike film S_3, the unavoidable Ru deficiency in film S_2 remains sufficiently low, ensuring that the electronic properties of $Nd_2Ru_2O_7$ are not compromised.

IV. CONCLUSION

In conclusion, we have successfully developed a modified reactive off-axis sputtering technique utilizing two metal targets, proving effective for the growth of epitaxial films of $Nd_2Ru_2O_7$. This method holds great potential for the fabrication of epitaxial films of other pyrochlore ruthenates. Our findings open up possibilities for exploring the exotic electronic and magnetic properties of these materials using state-of-the-art experimental techniques that require a large sample surface area. The ability to manipulate and control these properties in thin film form presents avenues for developing innovative devices and technologies based on pyrochlore ruthenates. We have also shown that our sputtering method allows tight control of the stoichiometry, and that the optical spectra can serve as a sensitive diagnostic of the Ru vacancy concentration. These capabilities may prove useful for applications of pyrochlore ruthenates in electrocatalysis.

ACKNOWLEDGMENTS

We gratefully acknowledge T.T.H. Tran and C. Busch for their assistance with XRD and SEM-EDX measurements, and F.V.E. Hensling for helpful discussions. We thank B. Stuhlhofer, P. Specht, B. Bruha, and M. Schulz for technical support. Special thanks to A. Steinman for his assistance in 3D design and figure creation. The project was supported by the European Research Council under Advanced Grant No. 669550 (Com4Com) and by the German Research Foundation (DFG) through TRR360 (Project No. 492547816).

[1] D. F. Abbott, R. K. Pittkowski, K. Macounová, R. Nebel, E. Marelli, E. Fabbri, I. E. Castelli, P. Krtil, and T. J. Schmidt, Design and synthesis of ir/ru pyrochlore catalysts for the oxygen evolution reaction based on their bulk thermodynamic properties, ACS Appl. Mater. Interfaces **11**, 37748 (2019).

[2] P. Gayen, S. Saha, and V. Ramani, Pyrochlores for advanced oxygen electrocatalysis, Acc. Chem. Res. **55**, 2191 (2022).

[3] J. G. Rau and M. J. P. Gingras, Frustrated quantum rare-earth pyrochlores, Annu. Rev. Condens. Matter Phys. **10**, 357 (2019).

[4] C. R. Wiebe and A. M. Hallas, Frustration under pressure: Exotic magnetism in new pyrochlore oxides, APL Mater. **3**, 041519 (2015).

[5] W. Witczak-Krempa, G. Chen, Y. B. Kim, and L. Balents, Correlated quantum phenomena in the strong spin-orbit regime, Annu. Rev. Condens. Matter Phys. **5**, 57 (2014).

[6] Y. Li, T. Oh, J. Son, J. Song, M. K. Kim, D. Song, S. Kim, S. H. Chang, C. Kim, B.-J. Yang, and T. W. Noh, Correlated magnetic weyl semimetal state in strained $Pr_2Ir_2O_7$, Adv. Mater. **33**, 2008528 (2021).

[7] T. Ohtsuki, Z. Tian, A. Endo, M. Halim, S. Katsumoto, Y. Kohama, K. Kindo, M. Lippmaa, and S. Nakatsuji, Strain-induced spontaneous Hall effect in an epitaxial thin film of a luttinger semimetal, Proc. Natl. Acad. Sci. USA **116**, 8803 (2019).

[8] X. Liu, S. Fang, Y. Fu, W. Ge, M. Kareev, J.-W. Kim, Y. Choi, E. Karapetrova, Q. Zhang, L. Gu, E.-S. Choi, F. Wen, J. H. Wilson, G. Fabbris, P. J. Ryan, J. W. Freeland, D. Haskel, W. Wu, J. H. Pixley, and J. Chakhalian, Magnetic Weyl semimetallic phase in thin films of $Eu_2Ir_2O_7$, Phys. Rev. Lett. **127**, 277204 (2021).

[9] L. Guo, N. Campbell, Y. Choi, J.-W. Kim, P. J. Ryan, H. Huyan, L. Li, T. Nan, J.-H. Kang, C. Sundahl, X. Pan, M. S. Rzchowski, and C.-B. Eom, Spontaneous Hall effect enhanced by local Ir moments in epitaxial $Pr_2Ir_2O_7$ thin films, Phys. Rev. B **101**, 104405 (2020).

[10] W. J. Kim, J. Song, Y. Li, and T. W. Noh, Perspective on solid-phase epitaxy as a method for searching novel topological phases in pyrochlore iridate thin films, APL Mater. **10**, 080901 (2022).

[11] S. Lee, J.-G. Park, D. T. Adroja, D. Khomskii, S. Streltsov, K. A. McEwen, H. Sakai, K. Yoshimura, V. I. Anisimov, D. Mori, R. Kanno, and R. Ibberson, Spin gap in $Tl_2Ru_2O_7$ and the possible formation of Haldane chains in three-dimensional crystals, Nat. Mater. **5**, 471 (2006).

[12] M. Yoshida, M. Takigawa, A. Yamamoto, and H. Takagi, Metal–insulator transition and magnetic order in the pyrochlore oxide $Hg_2Ru_2O_7$, J. Phys. Soc. Jpn. **80**, 034705 (2011).

[13] A. Krajewska, A. Yaresko, J. Nuss, A. S. Gibbs, S. Bette, M. Blankenhorn, R. E. Dinnebier, D. P. Sari, I. Watanabe, J. Bertinshaw, H. Gretarsson, K. Ishii, D. Matsumura, T. Tsuji, M. Isobe, B. Keimer, H. Takagi, and T. Takayama, Formation of orbital molecules on a pyrochlore lattice induced by A-O bond covalency, arXiv:2111.05057 [cond-mat.str-el].

[14] J. Kim, P.-C. Shih, K.-C. Tsao, Y.-T. Pan, X. Yin, C.-J. Sun, and H. Yang, High-performance pyrochlore-type yttrium ruthenate electrocatalyst for oxygen evolution reaction in acidic media, J. Am. Chem. Soc. **139**, 12076 (2017).

[15] G. Kim, Y. E. Suyolcu, J. Herrero-Martin, D. Putzky, H. P. Nair, J. P. Ruf, N. J. Schreiber, C. Dietl, G. Christiani, G. Logvenov, M. Minola, P. A. van Aken, K. M. Shen, D. G. Schlom, and B. Keimer, Electronic and vibrational signatures of ruthenium vacancies in Sr_2RuO_4 thin films, Phys. Rev. Mater. **3**, 094802 (2019).

[16] G. Kim, K. Son, Y. E. Suyolcu, L. Miao, N. J. Schreiber, H. P. Nair, D. Putzky, M. Minola, G. Christiani, P. A. van Aken, K. M. Shen, D. G. Schlom, G. Logvenov, and B. Keimer, Inhomogeneous ferromagnetism mimics signatures of the topological Hall effect in $SrRuO_3$ films, Phys. Rev. Mater. **4**, 104410 (2020).

[17] G. Kim, Spectroscopic investigation of defects and their impact on the physical properties of transition-metal-oxide heterostructures, Ph.D. thesis, University of Stuttgart, 2020.

[18] C. B. Eom, J. Z. Sun, K. Yamamoto, A. F. Marshall, K. E. Luther, T. H. Geballe, and S. S. Laderman, *In situ* grown $YBa_2Cu_3O_{1-\delta}$ thin films from single target magnetron sputtering, Appl. Phys. Lett. **55**, 595 (1989).

[19] M. Ito, Y. Yasui, M. Kanada, H. Harashina, S. Yoshii, K. Murata, M. Sato, H. Okumura, and K. Kakurai, Neutron diffraction study of pyrochlore compound $R_2Ru_2O_7$ (R=Y, Nd) above and below the spin freezing temperature, J. Phys. Soc. Jpn. **69**, 888 (2000).

[20] M. W. Gaultois, P. T. Barton, C. S. Birkel, L. M. Misch, E. E. Rodriguez, G. D. Stucky, and R. Seshadri, Structural disorder, magnetism, and electrical and thermoelectric properties of pyrochlore $Nd_2Ru_2O_7$, J. Phys.: Condens. Matter **25**, 186004 (2013).

[21] S.-W. Chen, S.-W. Fu, C.-W. Pao, J.-M. Lee, S.-A. Chen, S.-C. Haw, J.-F. Lee, C.-H. Liu, C.-K. Chang, Y.-C. Chuang, H.-S. Sheu, K.-T. Lu, S.-T. Ku, L.-J. Chang, and J.-M. Chen, Low temperature structural anomalies arising from competing exchange interactions in pyrochlore $Nd_2Ru_2O_7$ probed by XRD and EXAFS, Phys. Chem. Chem. Phys. **17**, 23667 (2015).

[22] S. T. Ku, D. Kumar, M. R. Lees, W.-T. Lee, R. Aldus, A. Studer, P. Imperia, S. Asai, T. Masuda, S. W. Chen, J. M. Chen, and L. J. Chang, Low temperature magnetic properties of $Nd_2Ru_2O_7$, J. Phys.: Condens. Matter **30**, 155601 (2018).

[23] T. C. Fujita, Y. Kozuka, M. Uchida, A. Tsukazaki, T. Arima, and M. Kawasaki, Odd-parity magnetoresistance in pyrochlore iridate thin films with broken time-reversal symmetry, Sci. Rep. **5**, 9711 (2015).

[24] W. C. Yang, Y. T. Xie, X. Sun, X. H. Zhang, K. Park, S. C. Xue, Y. L. Li, C. G. Tao, Q. X. Jia, Y. Losovyj, H. Wang, J. J. Heremans, and S. X. Zhang, Stoichiometry control and electronic and transport properties of pyrochlore $Bi_2Ir_2o_7$ thin films, Phys. Rev. Mater. **2**, 114206 (2018).

[25] X. Liu, F. Wen, E. Karapetrova, J.-W. Kim, P. J. Ryan, J. W. Freeland, M. Terilli, T.-C. Wu, M. Kareev, and J. Chakhalian, *In-situ* fabrication and transport properties of (111) YIr_2O_7 epitaxial thin film, Appl. Phys. Lett. **117**, 041903 (2020).

[26] J. A. Woollam Co., *Guide to using WVASE32®: Spectroscopic Ellipsometry Data Acquisition and Analysis Software* (J.A. Woollam Co., Inc., Lincoln, Nebraska, 2012).

[27] A. N. Yaresko, V. N. Antonov, and P. Fulde, Localized U $5f$ electrons in UPd_3 from LDA + U calculations, Phys. Rev. B **67**, 155103 (2003).

[28] V. Antonov, B. Harmon, and A. Yaresko, *Electronic Structure and Magneto-Optical Properties of Solids* (Kluwer Academic Publishers, Dordrecht, Boston, London, 2004).

[29] C. R. Stanek, L. Minervini, and R. W. Grimes, Nonstoichiometry in $A_2B_2O_7$ pyrochlores, J. Am. Ceram. Soc. **85**, 2792 (2002).

[30] F. V. E. Hensling, D. Dahliah, P. Dulal, P. Singleton, J. Sun, J. Schubert, H. Paik, I. Subedi, B. Subedi, G.-M. Rignanese, N. J. Podraza, G. Hautier, and D. G. Schlom, Epitaxial stannate pyrochlore thin films: Limitations of cation stoichiometry and electron doping, APL Mater. **9**, 051113 (2021).

[31] G. Sala, M. J. Gutmann, D. Prabhakaran, D. Pomaranski, C. Mitchelitis, J. B. Kycia, D. G. Porter, C. Castelnovo, and J. P. Goff, Vacancy defects and monopole dynamics in oxygen-deficient pyrochlores, Nat. Mater. **13**, 488 (2014).

[32] B. Dabrowski, O. Chmaissem, P. W. Klamut, S. Kolesnik, M. Maxwell, J. Mais, Y. Ito, B. D. Armstrong, J. D. Jorgensen, and S. Short, Reduced ferromagnetic transition temperatures in $SrRu_{1-v}O_3$ perovskites from Ru-site vacancies, Phys. Rev. B **70**, 014423 (2004).

[33] D. Saito, K. Kaminaga, D. Oka, and T. Fukumura, Itinerant ferromagnetism in rocksalt NdO epitaxial thin films, Phys. Rev. Mater. **3**, 064407 (2019).

[34] E.-M. Anton, J. F. McNulty, B. J. Ruck, M. Suzuki, M. Mizumaki, V. N. Antonov, J. W. Quilty, N. Strickland, and H. J. Trodahl, NdN: An intrinsic ferromagnetic semiconductor, Phys. Rev. B **93**, 064431 (2016).

[35] J. M. Leger, N. Yacoubi, and J. Loriers, Synthesis of neodymium and samarium monoxides under high pressure, Inorg. Chem. **19**, 2252 (1980).

[36] D. G. Schlom, L.-Q. Chen, C. J. Fennie, V. Gopalan, D. A. Muller, X. Pan, R. Ramesh, and R. Uecker, Elastic strain engineering of ferroic oxides, MRS Bull. **39**, 118 (2014).

[37] M. Ito, Y. Yasui, M. Kanada, H. Harashina, S. Yoshii, K. Murata, M. Sato, H. Okumura, and K. Kakurai, Nature of spin freezing transition of geometrically frustrated pyrochlore system $R_2Ru_2O_7$ (R=rare earth elements and Y), J. Phys. Chem. Solids **62**, 337 (2001).

[38] E.-M. Köck, M. Kogler, T. Bielz, B. Klötzer, and S. Penner, *In situ* FT-IR spectroscopic study of CO_2 and CO adsorption on Y_2O_3, ZrO_2, and yttria-stabilized ZrO_2, J. Phys. Chem. C **117**, 17666 (2013).

[39] R. A. Pawar, A. K. Nikumbh, D. S. Bhange, N. J. Karale, D. V. Nighot, and M. B. Khanvilkar, Chemical synthesis and characterization of nano-sized rare-earth ruthenium pyrochlore compounds $Ln_2Ru_2O_7$ (Ln= rare earth), Bull. Mater. Sci. **40**, 1335 (2017).